

**Assembly and disassembly of Rad51 filaments on single-stranded DNA: A novel assay to study the dynamics of protein-ssDNA interactions at the single-molecule level**

Authors: Mariella Franker  
Submitted: 4. July 2016  
Published: 4. July 2016  
Volume: 3  
Issue: 3  
Keywords: Rad51 filaments, single-stranded DNA, protein-ssDNA interactions, biomolecular sciences, master thesis  
DOI: 10.17160/josha.3.3.198

**JOSHA**

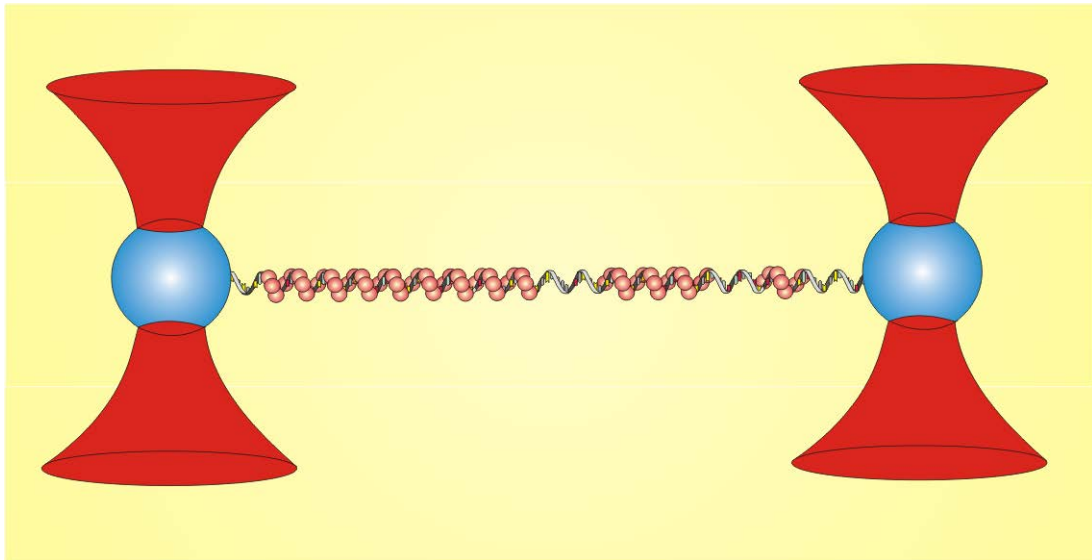
[josha.org](http://josha.org)

**Journal of Science,  
Humanities and Arts**

JOSHA is a service that helps scholars, researchers, and students discover, use, and build upon a wide range of content

# Assembly and disassembly of Rad51 filaments on single-stranded DNA:

A novel assay to study the dynamics of protein-ssDNA interactions at  
the single-molecule level



Mariella Franker

Student number: 1465465

Biomolecular Sciences, Cell Biology

April – December 2009, 36 ECTS

Physics of Complex Systems, Vrije Universiteit Amsterdam

Daily Supervisor: Andrea Candelli, M.Sc.

Project Supervisor: Dr. Ir. Erwin Peterman

# Table of contents

|  |           |
|--|-----------|
| <b>Summary</b> .....                                     | <b>3</b>  |
| <b>Chapter 1 Introduction</b> .....                      | <b>4</b>  |
| DNA damage repair .....                                  | 4         |
| Rad51 nucleoprotein filament .....                       | 7         |
| Mechanical properties of DNA .....                       | 8         |
| <b>Chapter 2 Experimental setup</b> .....                | <b>11</b> |
| Principles of optical trapping .....                     | 11        |
| Optical trapping and fluorescence microscopy setup ..... | 12        |
| DNA construct .....                                      | 14        |
| <b>Chapter 3 Results</b> .....                           | <b>16</b> |
| Filament stability .....                                 | 16        |
| Nucleation .....   | 17        |
| Assembly .....   | 18        |
| Disassembly .....  | 19        |
| Force data .....   | 19        |
| <b>Chapter 4 Discussion</b> .....                        | <b>22</b> |
| <b>Conclusion</b> .....                                  | <b>25</b> |
| <b>References</b> .....                                  | <b>26</b> |
| <b>Appendix</b> .....                                    | <b>28</b> |

## Summary

Eukaryotic recombinase protein Rad51 is the key player in homologous recombination, an essential DNA repair mechanism used for the repair of double-strand breaks. Double-strand breaks can lead to chromosome fragmentation and are particularly hazardous during and shortly after DNA replication. The mechanism of homologous recombination is highly conserved between species and recombinase proteins are expressed in a wide range of prokaryotic and eukaryotic cells. The primary event in homologous recombination is the formation of a helical nucleoprotein filament on single-stranded DNA overhangs around double-strand breaks. The nucleoprotein filament mediates all subsequent steps of homologous recombination and is capable of performing strand exchange reactions unassisted *in vitro*. Dynamic assembly and disassembly interactions between the nucleoprotein filament and its DNA substrate are essential for strand exchange. Investigating the Rad51 – single-stranded DNA complex presents numerous challenges and it has never been observed directly. This study presents a novel assay to investigate these interactions at the single-molecule level. A combination of dual-beam optical trapping and high-resolution fluorescence microscopy allows *in situ* creation and manipulation of single-stranded DNA molecules, while at the same time binding of fluorescently labeled Rad51 proteins can be observed directly. Using this novel single-molecule approach, it is possible to distinguish between the different steps of filament formation: nucleation, extension and disassembly. We are able to simultaneously interrogate the molecular mechanisms of filament assembly and disassembly, and determine nucleation, extension and disassembly rates as well as binding unit sizes without any *a priori* assumptions. Furthermore, we are able to investigate the effects of tension on the various stages of filament formation and observe Rad51-induced forces in real time.

## Chapter 1 Introduction

Recombinase protein Rad51 is the key player in homologous recombination in Eukaryotic cells. This essential DNA damage repair mechanism uses a homologous sequence to repair double-strand breaks (DSBs) without any loss of genetic information (1). The key event in the process is the formation of a helical filament on single-stranded DNA (ssDNA) overhangs around the ends of the double-strand break. During binding, the filament exerts force on the DNA substrate (2). The dynamic association and dissociation of the filament and the forces induced on the DNA template are essential for filament function. This first chapter describes the general mechanism of homologous recombination and highlights the many regulatory proteins involved in the process *in vivo*. Structure and function of the Rad51 nucleoprotein filament are considered in more detail, as well as the effects of Rad51 binding on the mechanical properties of DNA. Chapter 2 discusses the principles of optical trapping and the experimental procedure. In the final chapters 3 and 4, I discuss a series of preliminary experiments investigating Rad51 filament formation and dissociation on single-stranded DNA.

### DNA damage repair

DNA damage occurs throughout a cell's lifetime and efficient repair is essential to maintain genomic integrity. Various internal and external factors such as toxins, viruses, radiation, DNA nucleases, reactive oxygen species and drugs can damage DNA. Physical stress can also induce DNA damage, for example when chromosomes are pulled to opposite ends of the cell during mitosis. DNA damage varies from single base mutations and ruptures in single DNA strands to complete cleavage of both strands, a severe type of damage called double-strand breaks (DSBs). Besides accidental damage, eukaryotic cells express specialized endonucleases that purposely induce DSBs during meiosis. These induced breaks facilitate immunoglobulin diversity in B-cells (V(D)J switching) and are essential for proper chromosome segregation (3)(4). Detection of DNA damage initiates complex phosphorylation cascades that activate various protection pathways inside the cell. The first proteins to respond are those of the MR(X)N-complex (Mre11, Rad50 and Xrs2/Nbs1 proteins). This complex serves as a DNA-damage sensor and acts as a scaffold to hold the double-strand break ends together (5), a mechanism that is particularly important *in vivo* when the broken ends risk drifting apart. The MR(X)N-complex recruits and activates ATM/ATR transducer kinases that play a central role in cell cycle arrest (6). The cell is ushered into a quiescent state to prevent faulty DNA replication and to allow enough time for proper repair. Histone modification proteins phosphorylate surrounding histones to amplify the DNA damage signal. Modified histones are found in extended regions on both sides of the break and recruit and activate other important proteins involved in the processes (7). Finally, repair proteins are recruited to the break site. The cell employs two different mechanisms to repair DSBs: non-homologous end-joining (NHEJ) and homologous recombination. NHEJ simply fuses the two ends of a DSB together. In some cases, a few nucleotides are resected around the break ends. If this occurs in an important protein-encoding region, vital genetic information is lost and this can have deleterious effects on the cell. In most cases, however, double-strand breaks are efficiently repaired by NHEJ in different stages of the cell cycle. Non-homologous end-joining nonspecifically repairs double-strand breaks regardless of homology and it is considered to be the most robust DSB repair mechanism (8). Homologous recombination on the other hand, requires a homologous sequence to properly repair the break. A specialized nucleoprotein filament

is formed on ssDNA around the break and aligns the broken strand with a homologous duplex DNA, usually the sister chromatid. The duplex DNA is invaded and the broken strand is paired with its complementary sequence and repaired. Accurate repair is particularly critical during and shortly after DNA replication (S and G2 phase) and it is during these stages that homologous recombination out-competes NHEJ.

Homologous recombination can broadly be divided into three stages: (i) initiation and filament formation, (ii) homology search and strand exchange and (iii) branch migration and resolution (figure 1.1) (9). During initiation, specialized exonucleases resect the DSB ends in 5' to 3' direction creating single-stranded DNA overhangs. Any exposed ssDNA inside cells is immediately bound by single-strand binding proteins (RPAs and SSBs). These proteins remove secondary structures of ssDNA and prevent unwanted interactions with proteins and structures inside the cell. Recombinase proteins, Rad51 in eukaryotes and RecA in prokaryotes, are loaded onto these ssDNA overhangs and a right-handed helical filament is formed around the DNA. The nucleoprotein filament mediates all subsequent steps of homologous recombination and is capable of performing strand exchange unassisted *in vitro*. *In vivo*, however, many mediator proteins regulate the process. Rad52 proteins remove RPAs and assist Rad51 loading on ssDNA (9). Protein complexes, such as Rad51B-Rad51C and Hop2-Mnd1 heterodimers, stabilize the filament prior to and during strand exchange (10) (11). One important recombinase mediator in humans is tumor suppressor protein BRCA2 (12). This 390 kDa protein contains several structural motifs that specifically bind Rad51. Through these interactions, BRCA2 is thought to be involved in all stages of filament formation: loading or nucleation of Rad51, oligomerization and disassembly. Once formed, the nucleoprotein filament searches the sister chromatid for a homologous region. It is still unclear how this happens with the high efficiencies observed *in vivo*. Several models have been proposed that include random collisions between filament and DNA, 1D random walk and unidirectional diffusion. Some models speculate that pairing between homologous sequences occurs prior to DNA damage. Homologous regions are supposedly kept in close proximity by specialized structures in the nucleus such as telomere and centromere clusters, *cis*-acting pairing centers and so called repair hubs (13) (14). Once a homologous region is found, the filament aligns the broken strand with its complementary region and invades the duplex DNA (D-loop structure in figure 1.1.a). The physical mechanism behind these interactions is not well understood. Presumably, first a paranemic joint is formed where the strands are paired but not yet topologically linked. It is proposed that the filament rotates the bases of the duplex DNA out of their stacked conformation in order to 'sample' the duplex for homology (15). A sufficiently high A:T-content is essential for homology recognition, arguing in favor of this model. Once a stable match has been formed, the strands are Watson-Crick base-paired (plectonemic joint formation) and DNA polymerases and ligases repair the broken strand. At this point, the D-loop can simply be unwound to yield only non-crossover products in the synthesis-dependent strand annealing model (SDSA, figure 1.1.b), or the second end can be captured and a branched intermediate state with two Holliday junctions (HJ) is formed (double-strand break-repair model (DSBR), figure 1.1.c). Studies have shown that Rad52 is also involved in second end capture (16). At this stage, branch migration can occur and the junctions are moved along the DNA to lengthen or shorten the newly formed duplex. Molecular motor proteins such as helicases and Rad54 are known to induce forces up or downstream of the Holliday junction that push the junction(s) along the DNA (8). Rad54 induced forces play a role in multiple stages of homologous recombination including chromatin remodeling, homology search, and filament disassembly. In the final resolution stage, the Holliday junctions are cut by specialized resolvase enzymes to yield crossover or non-crossover products.

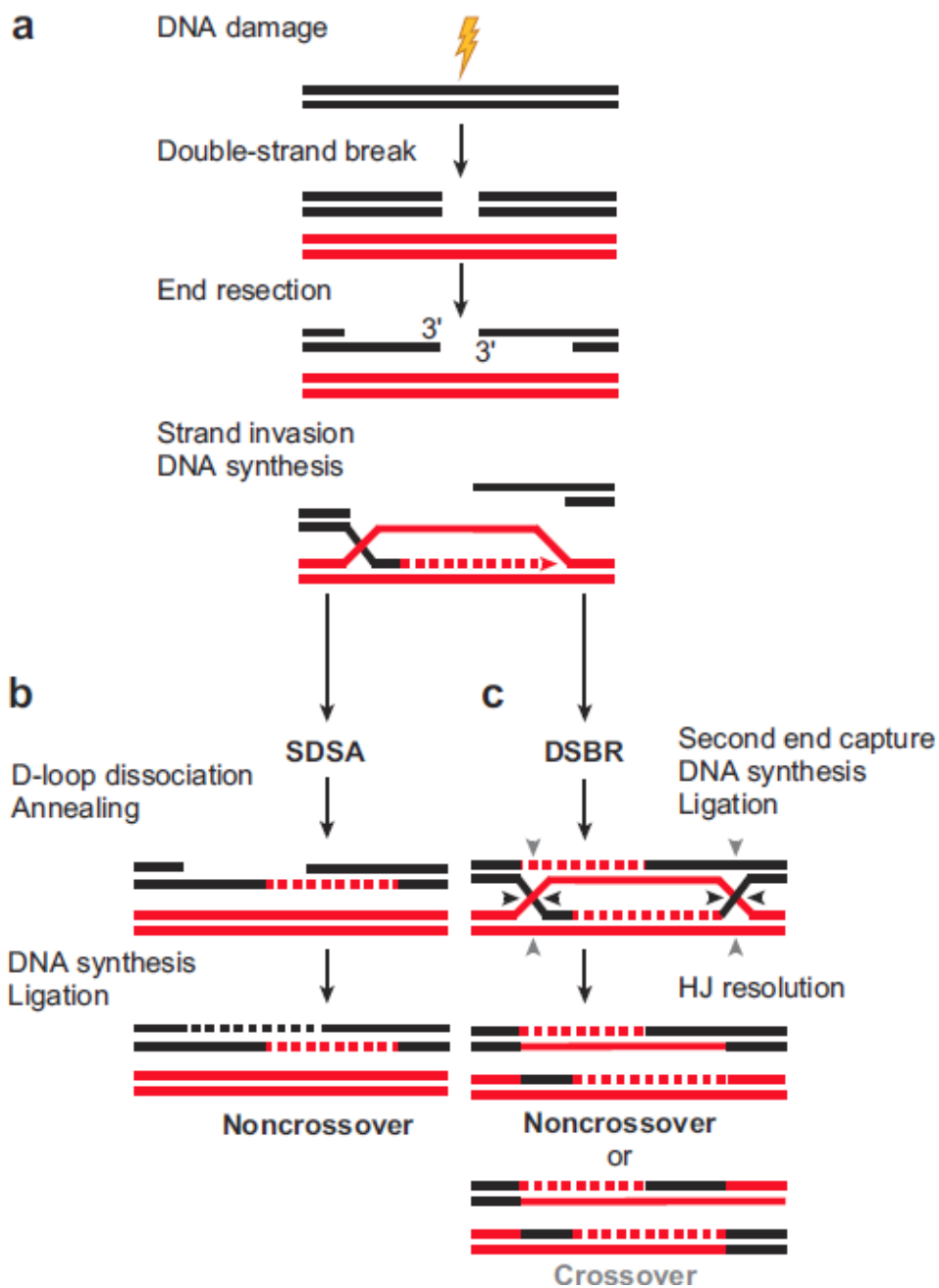


**Figure 1.1 Mechanism of homologous recombination** (9). The MR(X)N-complex binds double-strand break (DSB) ends and initiates various protection and repair pathways. Exonucleases resect the DSB ends and create ssDNA overhangs with exposed 3-OH ends. Rad51 proteins are loaded onto these ssDNA regions and form a helical nucleoprotein filament around the DNA. The Rad51 filament searches the sister chromatid for homology and facilitates strand invasion (D-loop formation). DNA polymerase and ligase repair the broken strand. Unwinding of the D-loop yields non-crossover products in SDSA pathway. Alternatively, the second end is captured and two Holliday junctions (HJ) are formed. Cutting enzymes yield crossover or non-crossover products (small arrows) in DSBR pathway. (SDSA = synthesis-dependent strand annealing model, DSBR = double-strand break-repair model)

## Rad51 nucleoprotein filament

The nucleoprotein filament is the driving force behind homologous recombination. The core domain of recombinase proteins (figure 1.2.a) is highly conserved between species and shows strong homology with  $F_1$ -ATPases and DNA helicases (17). The monomer structure contains a P-loop that coordinates binding of ATP and a divalent ion. Flexible loops are involved in DNA binding and may also play a role in Rad51 oligomerization and in interaction with recombination mediators. The nucleotide binding site is located on the subunit-subunit interface between two monomers and strong allosteric coupling is found between ATP binding, DNA binding and ATP hydrolysis (18) (19). Binding of the nucleotide increases affinity for DNA while ATP hydrolysis reduces DNA affinity and triggers disassembly. Bulk biochemistry studies have shown that Rad51 has similar binding affinity for ssDNA and dsDNA (17). The filament forms a right-handed helical structure around the DNA template. *In vivo*, the filament can grow up to several kilobases long and it mediates all subsequent steps of homologous recombination. Figure 1.2.b shows the crystal structure of an active Rad51 filament in the presence of single-stranded DNA and a slowly hydrolysable ATP-analog (ATP- $\gamma$ -S) (2). Each Rad51 monomer binds 3 bases and the filament contains ~6 Rad51 and ~18-19 bases per helical turn. The DNA lies along the filament axis (black line) and is partly unwound and extended to ~150% of B-form DNA. This structure shows monomers bound to each other with slightly alternating surfaces. Contrary to previous accounts, this indicates that the functional unit within the filament may be a dimer and that the true symmetry is three-fold instead of six-fold (2).

Filament formation is roughly divided into three steps: nucleation, extension, and disassembly (figure 1.2.c). First, a protein or a group of proteins bind to the DNA to form a small nucleation site. This stage is relatively slow and is the rate-limiting step in filament formation. Nucleation events are easily controlled by altering the nature of nucleotide cofactors and by altering protein or salt concentrations, indicating that this is an important regulatory step *in vivo* (20) (21). Recombinase proteins bind cooperatively and once a stable nucleus has formed, the filament rapidly grows by binding additional proteins at the filament ends. After ATP hydrolysis, recombinase proteins lose affinity for DNA and dissociate from the substrate. There is an ongoing debate about the actual sizes of the different binding units. Single-molecule fluorescence and magnetic tweezer experiments indicate that nucleation happens in complexes of 3-5 Rad51 (22) (23). Formation of multimers in solution would increase binding affinity for DNA and stimulate nucleation. FRET and single-molecule fluorescence experiments indicate that extension occurs by binding of dimers or monomers to the pre-existing filament on dsDNA (22) (24).

Interestingly, both the prokaryotic and eukaryotic filament is found in different isoforms. The occurrence of these slightly different structures depends on the available cofactors bound to the core of the recombinase proteins (25). The active Rad51 filament with ATP and  $Mg^{2+}$  bound at its center is relatively extended (pitch ~83-130 Å) when compared to the inactive filament with ADP bound (pitch ~65-85 Å). It is proposed that prior to dissociation, the filament rapidly switches from an ATP-bound conformation to an ADP-bound state, and condenses while remaining bound to the DNA (26). These dynamic interactions are thought to be essential for strand exchange. In the most widely accepted strand-exchange model, the filament does not merely have a DNA-pairing function but also actively performs strand exchange when triggered by hydrolysis (27).

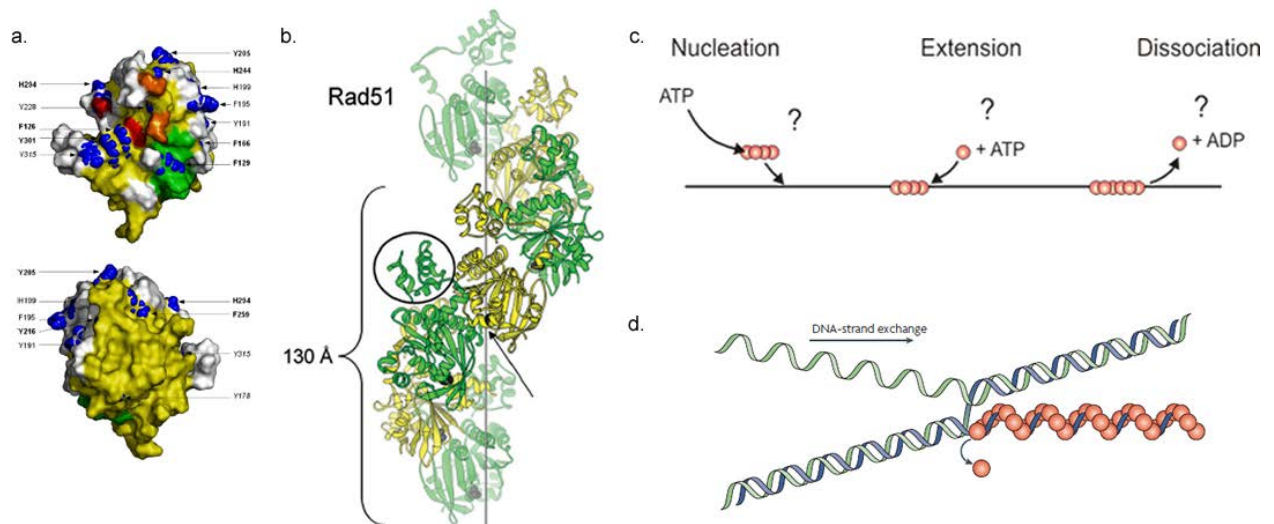


**Figure 1.2 a) Rad51 core domain** (19). The core domain structure of recombinase proteins is highly conserved between species. A P-loop structure (green) coordinates binding of ATP and a divalent ion. This nucleotide binding site is found on the subunit-subunit interface (white) between adjacent monomers. Flexible loops L1 and L2 (orange and red, respectively) bind the DNA template and may be involved in signaling to recombination mediators. The core structure is shown from the inside of the filament (top image) and from the outside of the filament (bottom image). **b) Crystal structure of Rad51 filament** (2). Crystals were grown in the presence of ATP- $\gamma$ -S and ssDNA. The active (ATP/  $Mg^{2+}$ -bound) filament extends B-form DNA to ~150% of its original length. The DNA lies along the filament axis (black line) and the nucleotide binding site is indicated with a black arrow. **c) Dynamics of filament formation.** Filament formation is divided into three steps: nucleation, extension and dissociation. First a small nucleation spot is formed when Rad51 proteins first bind to the DNA. Additional proteins cooperatively bind to the end of the pre-existing filament during extension. When ATP is hydrolyzed, the proteins dissociate from the DNA substrate. The sizes of the various binding units are still unknown (indicated with question marks). **d) Strand exchange model.** Dynamic interactions between assembly and disassembly are thought to be essential for strand exchange. The Rad51 filament has a DNA pairing function and actively promotes strand exchange when triggered by ATP hydrolysis.

### Mechanical properties of DNA

Mechanical tension in the DNA substrate plays an important role in recombinase protein function. The DNA polymer is a flexible, yet very strong molecule. Nick-free DNA can withstand forces over 100 pN without shearing (28) and its flexible double helical structure allows it to be wrapped and condensed inside the nucleus to nearly 10,000 times its original length. Using dual optical traps, force can be exerted on a single DNA molecule in a controlled manner by pulling along the DNA axis (figure 1.3, top image). Such experiments produce characteristic force-stretching curves (figure 1.3, bottom image). For dsDNA, this behavior has traditionally been described with Worm-Like Chain models (WLC). The WLC model is applicable to Hookean springs; that is inextensible, isotropic rods for which induced stress is directly proportional to the applied strain according to an elastic stretch modulus. The elastic stretch modulus determined for dsDNA is ~1300 pN (29). In solution, dsDNA is flexible and bends locally due to thermal fluctuations. This bending is purely entropic and when pulling on the DNA molecule, initially its secondary structure is removed and its entropic fluctuations are limited. The WLC model accurately describes dsDNA behavior up to forces of ~20 pN. Above 20 pN, force is exerted on the DNA backbone, deforming it from its regular B-form. Now the DNA is no longer inextensible and its contour length increases. This behavior can be modeled by adding an enthalpic factor to the WLC model, providing us with the Extensible Worm-Like Chain model (EWLC). Figure 1.3 shows the force-stretching curve of a dsDNA molecule fit by EWLC model with a stretch

modulus of 2000 pN (bottom image, green line). Around 65 pN another aberrant behavior is observed. The dsDNA now enters the overstretching plateau. During this regime B-form DNA is extended up to 70% beyond its contour length. Two competing models have been proposed to describe the structure of this intermediate state. One model proposes that the double helix is slowly unwound while the complementary base-pairing remains intact. A second model suggests that the hydrogen bonds between the duplex are broken and two single DNA strands are formed. A recent study showed that the second model is applicable and that this transition closely resembles thermal melting (28). Force-stretching behavior of ssDNA can be accurately modeled as a simple freely-jointed chain (figure 1.3, bottom image, blue line). Each base can be considered an inextensible, rigid segment connected by flexible hinges.

Binding of recombinase proteins greatly alter the DNA mechanical properties. Studies performed on the prokaryotic RecA filament have shown that the nucleic acid component of the filament accounts for most of its stretch modulus while the persistence length and bending rigidity are dominated by the protein component (30). Persistence length and stretch modulus of DNA-RecA filaments increase for both dsDNA and ssDNA when compared to naked DNA. The total stretch modulus obtained for the DNA-protein filament is greater than the sum of its individual parts, indicating that bound recombinase proteins stiffen the DNA. Furthermore, the stretch modulus of filaments bound by ATP is smaller than filaments bound by the slowly-hydrolyzable ATP- $\gamma$ -S. Rapid hydrolyzation removes a percentage of the DNA-protein interactions within the nucleoprotein filament (26). It is thought that the filament switches from an ATP-bound conformation to an ADP-bound state prior to dissociation from DNA. A single-molecule study showed pauses in the dissociation profile of Rad51 from dsDNA. They propose that Rad51 monomers are locked into their DNA-bound conformation by neighboring proteins. Monomers freely hydrolyze ATP inside the filament but remain loosely bound to DNA. Dissociation bursts of several proteins are observed when the terminal Rad51 hydrolyzes ATP and detaches from the template (26).

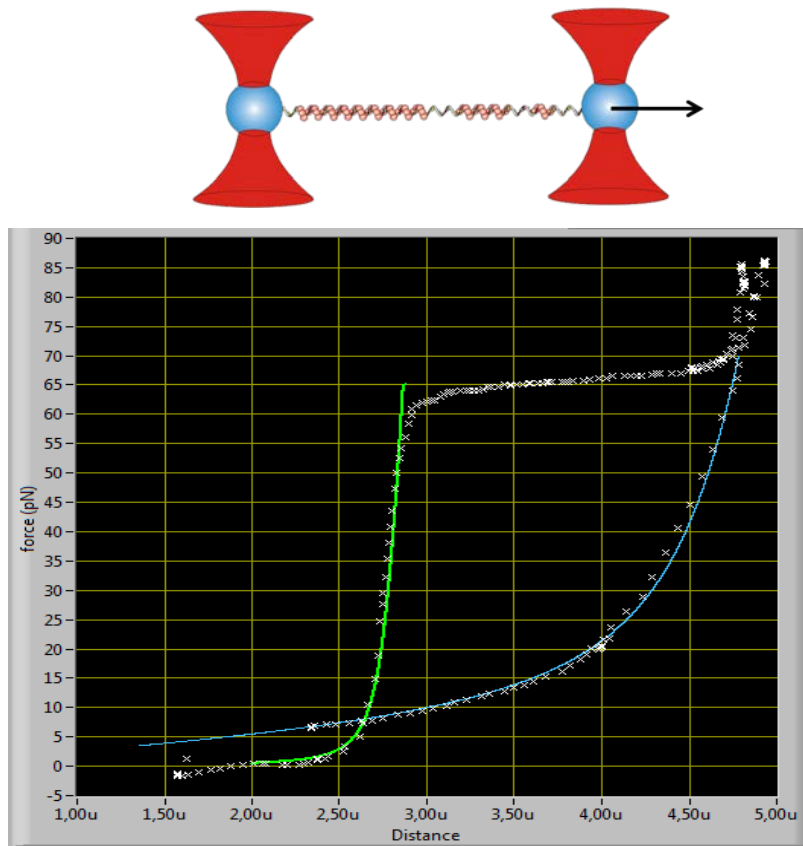


**Figure 1.3** Manipulating single DNA molecules using dual-beam optical traps. **Top image:** Illustration of a single DNA molecule caught between two optically trapped beads. By moving one of the traps in the x-direction (indicated with a black arrow), the relative distance between the beads increases and an axial force is exerted on the DNA. **Bottom image:** Force-distance curves of double-stranded and single-stranded DNA. Applying low axial tension on dsDNA initially constrains the entropic fluctuations of the DNA. At forces above 20 pN, the DNA backbone starts to extend and an enthalpic factor is added. This behavior can be described with the Extensible Worm-Like Chain model (EWLC) (*green line*; persistence length = 23 nm, stretch modulus = 2000 pN). At 65 pN the dsDNA enters the overstretching plateau. During this regime, B-DNA undergoes a melting process similar to thermal melting. When pulling beyond the overstretching plateau, the double-stranded DNA is fully melted and two single DNA strands are formed. Single-stranded DNA behavior can be modeled with the freely-jointed chain model (*blue line*; Kuhn length = 1, stretch modulus = 1497 pN).

## Chapter 2 Experimental setup

A custom-built setup was developed to combine dual-beam optical trapping and high-resolution fluorescence microscopy (26). Using this approach, we are able to create single-stranded DNA *in situ* by force-induced melting and directly observe binding of fluorescently labeled Rad51 to ssDNA to study the dynamics between assembly and disassembly interactions. This chapter describes the principles of optical trapping and the experimental setup used in these experiments.

### Principles of optical trapping

Optical traps are created by focusing a high power laser into a diffraction-limited focal spot using a high numerical aperture objective (N.A. = 1.2 - 1.4). Small dielectric objects, such as micron-sized polystyrene spheres, near this focal spot will experience forces towards the laser focus due to refraction and reflection of the incident photons (31) (32). When the bead diameter is significantly larger than the wavelength of light, simple ray optics can be applied. Figure 2.1.a shows the restoring forces that act on a bead trapped in the laser focus. Light that is reflected off the bead's surface is scattered backwards according to Snell's law. Since there must be an equal and opposite reaction following a momentum change this means that the bead feels a force of equal magnitude and in opposite direction to that of the scattered light. This creates a force (called the scattering force) that pushes the bead in the direction of light propagation. Near the trap focus a second force, the gradient force, is created. The laser beam is tightly focused into a small spot and forms a 2D Gaussian around the focus. Dielectric materials in such an inhomogeneous field will experience a force along the intensity gradient and are pushed toward the center of the trap. For stable trapping, the gradient force must exceed the scattering force. Rays at the edges of the objective lens contribute most to the trapping force and high N.A. objectives increase the trapping stiffness (see figure 2.1.a). In first approximation, an optical trap can be treated as a Hookean spring, where the restoring force on the bead is directionally proportional to the optical trap stiffness  $\kappa$  and the distance  $x$  between the trap and the bead center ( $F = -\kappa \times x$ ). Any change in the position of the bead will result in a deflection of the laser beam, allowing pN detection of forces exerted on the beads, for example caused by the biological system.

The optical trap's spring constant is commonly calibrated using power spectrum analysis (33). This method is preferred above theoretical methods since accurate calibration is achieved without *a priori* knowledge of particle diameter or solvent viscosity. Figure 2.1.b shows the power spectrum of a trapped bead. Beads in solution are subject to random motion by constant bombardment of solvent particles. Idealized Brownian motion, known as 'white noise', occurs at each frequency with equal probability and appears in the power spectrum as a constant (red line). This diffusive Brownian motion is described by the Langevin equation of motion. Inside the trap, the bead experiences thermal motion as well as a restoring force caused by the optical trap. The Langevin equation for the bead due to both these forces is given by:

$$F(t) = \gamma \frac{dx(t)}{dt} + \kappa x(t) \quad (1)$$

where  $F(t)$  represents the random thermal force,  $\gamma$  is the drag coefficient and  $\kappa$  is the optical trap stiffness. The power spectrum of idealized Brownian motion is given by:

$$S_F(f) = |\mathcal{F}^2(f)| = 4\gamma k_B T \quad (2)$$

where  $\mathcal{F}(f)$  is the Fourier transform of  $F(t)$ . The Fourier transform over this random thermal motion corresponds to the power spectrum of the displacement fluctuations.

$$S_x(f) = |\xi^2(f)| = \frac{k_B T}{\gamma \pi^2 (f_c^2 + f^2)} \quad (3)$$

where  $\xi(f)$  is the Fourier transform for  $x(t)$  and  $f_c$  is the corner frequency. The power spectrum depicts the contribution of motions with different frequencies to the random thermal force  $F(t)$ . At high frequencies, the restoring force of the trap is not strong enough to restrict the bead's motions. The bead does not 'feel' the confinement of the trap on short time scales and the power spectrum represents that of free diffusion. At low frequencies, the bead's motions are confined to the trap focus. In this case, low frequency fluctuations contribute less to the thermal motion of the bead (red line is lowered to black line in figure 2.1.b). The characteristic corner frequency  $f_c$  of the optical trap depicts the cut off frequency from which the bead's movements become confined and is a measure of the trap stiffness.

$$\kappa = \frac{2k_B T}{\pi S_o f_c} \quad \text{or} \quad \kappa = 2\pi\gamma f_c \quad (4)$$

where  $S_o = S_f$  for  $f \ll f_c$  and the power spectrum is constant.

### Optical trapping and fluorescence microscopy setup

Our setup combines dual-beam optical trapping with wide-field epifluorescence microscopy (figure 2.2) (26). With this system, a single DNA molecule can be caught between two polystyrene beads and forces can be measured and applied along the axis of the trapped DNA molecule with pN accuracy. At the same time, binding of fluorescently labeled proteins to the DNA can be observed directly. The setup contains a 3 Watt Nd:YVO<sub>4</sub> trapping laser emitting 1064 nm wavelength infrared light (figure 2.2). This wavelength is commonly used when working with biological samples since absorbance in aqueous solutions is low at this wavelength and damage to the sample is minimized. The laser beam is equally split into two beams using a polarizing beam splitter. The two beams can be steered independently in x, y and z direction using telescope lens systems placed in the beam paths. One trap is externally controlled with a joystick to pull and exert forces on the DNA molecule. The beams are expanded to fill the objective aperture and are projected onto the back focal plane of the condenser to obtain a tightly focused, diffraction-limited focal spot. The beams are then recombined with a beam splitter and a dichroic mirror DM2 couples the beams into a water-immersion objective with N.A. = 1.2. The intensity profile in the back focal plane of the condenser, which is imaged onto a quadrant photodiode (QPD), depends on the distance between the bead and the trap center, but is not affected when the traps are moved around in the sample.

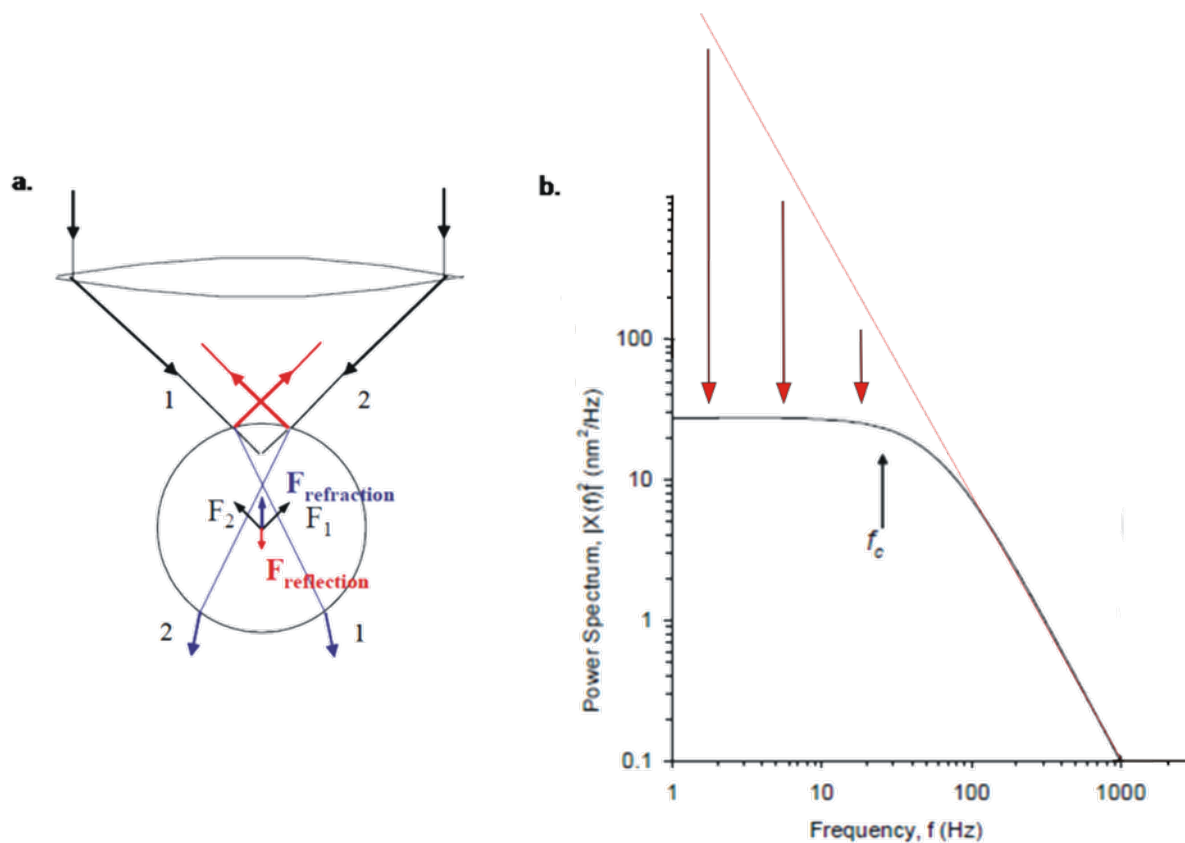


**Figure 2.1 Principles of optical trapping** (32). **a) Forces on an optically trapped bead.** Micron-sized polystyrene beads are trapped in the focus of a high power laser. Scattering forces caused by reflections off the bead surface push the bead in the direction of light propagation (red colored vectors). Dielectric materials in an inhomogeneous electric field experience a gradient force that pushes the bead towards the laser focus. For stable trapping, the gradient force must exceed the scattering force. The bead is trapped slightly downstream of the trap focus. **b) Ideal power spectrum of a trapped bead.** In solution, micron-sized beads are subject to random thermal motion (red line). Inside the trap a restoring force exists that restricts the bead's low frequency vibrations (black line). The characteristic corner frequency  $f_c$  is a measure for the optical trap stiffness.

A separate blue LED light source is coupled in via a dichroic mirror DM1 and illuminates the sample area. This bright-field image of the trapped beads is imaged onto a CCD camera and is used for real-time measurement of bead separation. Multiple fluorescence lasers can be mounted on the setup and can be successively coupled into the objective via dichroic mirrors (shown here as DM3). A fluorescence excitation laser emitting 532 nm light is used in these experiments to excite Alexa555 fluorophores. The fluorescence signal is imaged onto a sensitive electron multiplying CCD camera (EM-CCD). Although the size of the imaged fluorescent object is diffraction-limited, its center can be determined with arbitrary precision by calculating the point-spread function. Using this expression, single fluorophore precision is obtained.

A custom-built laminar flow cell system allows us to expose trapped molecules to different buffer-conditions within seconds (see inset figure 2.2). This specially designed flow cell has four parallel channels, each containing a different solution. Laminar flow creates invisible, non-physical barriers between these solutions. The traps are moved from one channel to the other, allowing 'quick dipping' of the DNA molecule in different solutions.

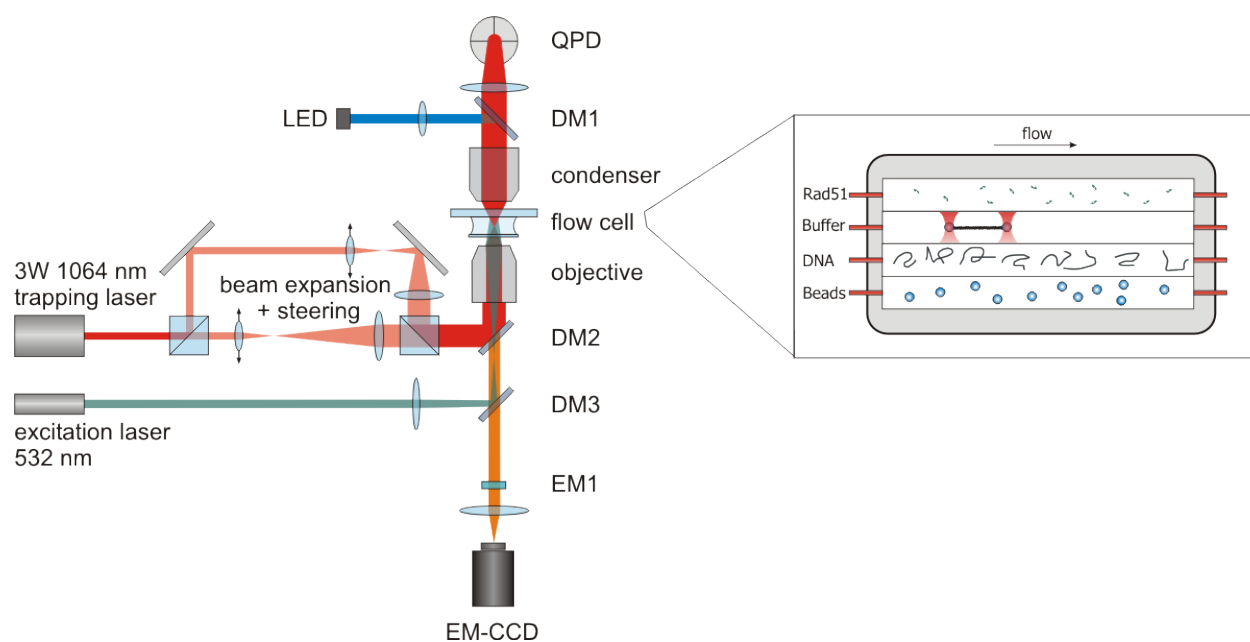


**Figure 2.2 Dual optical trap combined with wide-field epifluorescence microscopy** (26). The trapping laser beam is split into two beams that are individually controlled with beam steering elements. The beams are recombined and focused into the center of the flow cell with a high numerical aperture objective (N.A. = 1.2). The back focal plane of the condenser is projected onto a QPD for bead displacement measurements. A separate LED light source illuminates the sample area and the obtained bright-field image is coupled into a CCD camera for real-time measurement of bead separation. The fluorescence excitation light (here 532 nm) is coupled into the objective and imaged onto an electron multiplying CCD camera (EM-CCD). *Inset:* A custom built laminar flow cell system with multiple parallel channels allows rapid buffer exchanges. (For further details on buffers and experimental procedure see appendix).

### DNA construct

A short DNA construct of 8.3 kb was biotinylated on both ends of a single strand. With this construct a single-stranded DNA molecule is created inside the flow cell via force-induced melting. Figure 2.3 shows an overview of the biotinylation process. pKYB1 plasmids were purified from *E. coli* competent cells and cut with EcoRI restriction enzyme (step 1). This cutting enzyme specifically recognizes its DNA cutting sequence and produces short 5'-overhangs. Biotin-14-dATPs are incorporated at these overhangs by Klenow exo-polymerase (step 2). YM-50 column purification ensures that free nucleotides are removed from solution. The second strand is stripped of its biotinylated 3'-end by KpnI resection. Short, unbound biotinylated oligos are removed with column purification (step 3). In the final step, a biotinylated oligo primer is fused to the other end of the already biotinylated DNA strand. This oligo has a 24 nt overhang to aid in the melting process. Blunt-end ligation is achieved with T4 ligase. The final product is an 8.3 kb double-stranded DNA construct with biotin labels on both ends of the same strand. When stretched beyond the overstretching plateau (see figure 1.3, bottom image), the dsDNA fragment starts to melt at the 25 nt overhang. The dsDNA undergoes a transition much like thermal melting and the un-biotinylated strand is released into the surrounding solution and diffuses away. The remaining strand is bound on both sides by streptavidin-covered beads, allowing us to move and manipulate the molecule inside the flow cell.

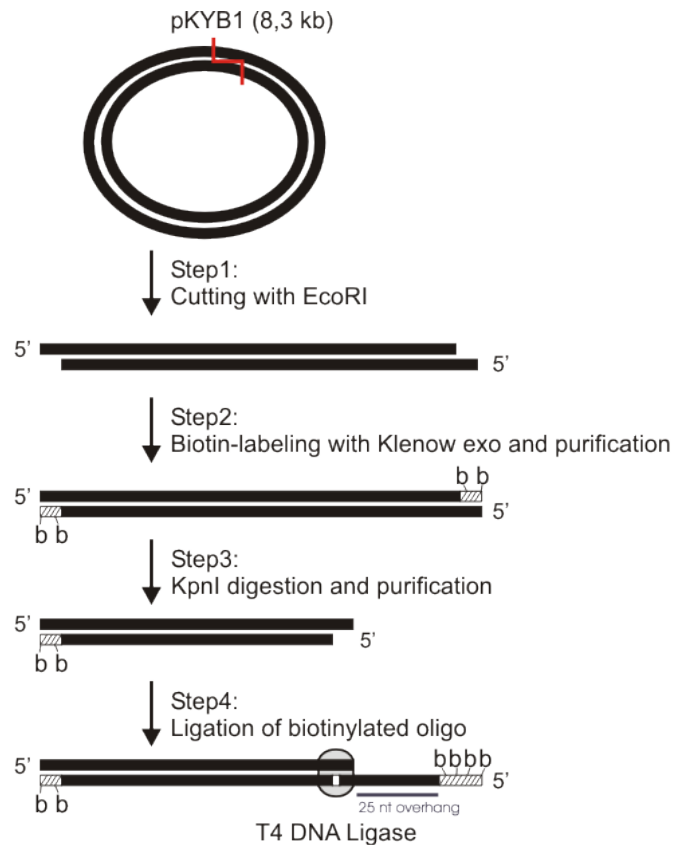


**Figure 2.3 Biotinylation process.** pKYB1 plasmids are amplified in *E.coli* competent cells, purified and biotinylated as follows. Step 1: EcoRI specifically cuts the plasmid and creates a linear product with short 3'-overhangs. Step 2: Klenow exo- binds the 3'-overhangs and incorporates biotin-14-dATPs. Step 3: KpnI removes the second biotinylated end. Step 4: T4 ligase ligates short biotinylated oligos to the exposed 5'-end. The oligo contains a 25 nt overhang to aid in the melting process. The final product is an 8.3 kb double-stranded DNA fragment with one DNA strand biotinylated on both ends. This dsDNA fragment can be caught between two streptavidin-covered beads and melted *in situ* at high force to create a single-stranded DNA molecule.

## Chapter 3 Results

This chapter discusses the first experiments done on Rad51 binding and unbinding from single-stranded DNA using this novel approach. Previously, bulk biochemistry studies and single-molecule fluorescence and magnetic tweezer experiments have been used to investigate the nucleoprotein filament, but it is difficult to resolve the exact mechanism of homologous recombination using these methods. Bulk experiments obscure intermediate protein states and it is impossible to study the mechano-chemical coupling of recombinase proteins using this approach. Magnetic tweezers have been used to monitor changes in DNA length due to Rad51 binding in real time; however, direct imaging of protein binding is not possible (23). Single-molecule fluorescence experiments using single-bead optical trapping have determined nucleation, extension, and disassembly rates for Rad51 binding on dsDNA (22) (26). However, studying Rad51 interactions on ssDNA is considerably more challenging and single-bead fluorescence experiments offer little information on force. Using our novel approach, it is possible to observe Rad51 binding on ssDNA directly and to investigate the mechanisms of filament assembly and disassembly. We can simultaneously investigate nucleation, extension and disassembly rates as well as binding unit sizes of the various stages without any *a priori* assumptions. Moreover, we are able to study the effects of tension on filament formation.

### Filament stability

In order to extract information about the biophysical properties of Rad51, we first performed a preliminary study to assess the stability of the filament and the photophysical properties of the fluorescent label. To address stability, ssDNA molecules were loaded with Rad51 in the presence of ATP and  $\text{Ca}^{2+}$  (assembly buffer) and fluorescence intensity was observed over time. Figure 3.1.a shows a fluorescence image of a Rad51 covered molecule immediately after incubation. Multiple large fluorescent patches of approximately 300-400 nm are visible along the entire length of the molecule. Graph 3.1.b shows fluorescence intensity over time. Previous single-molecule experiments have shown that Rad51 proteins remain tightly bound to dsDNA in the presence of  $\text{Ca}^{2+}$  for many minutes (21) (22). Our experiments show that  $\text{Ca}^{2+}$  stabilizes Rad51 on ssDNA as well, and that the filament is stable for up to 900s. In the first part of the experiment, the molecule was illuminated for 5s every 120s (strobing). The graph shows average values of fluorescence intensity over the full length of the DNA fragment during these 5s illuminations  $\pm$  Standard Deviation. The fluorescence intensity decreases over time with a decay rate  $k_1 = 9.7 \times 10^{-4} \text{ s}^{-1}$ . In the second part of the experiment, the same molecule was continuously illuminated for approximately 100s at the same optical density. Here, the decay rate is  $k_2 = 2.3 \times 10^{-2} \text{ s}^{-1}$ . Under these conditions, the molecule receives about 25 times more light during continuous illumination than during strobing. We observe that the fluorescence decay rates scale exactly with the laser exposure times (see inset), indicating that there is no disassembly of protein from the DNA and that any decrease in fluorescence intensity is due to photobleaching of the fluorescent label.

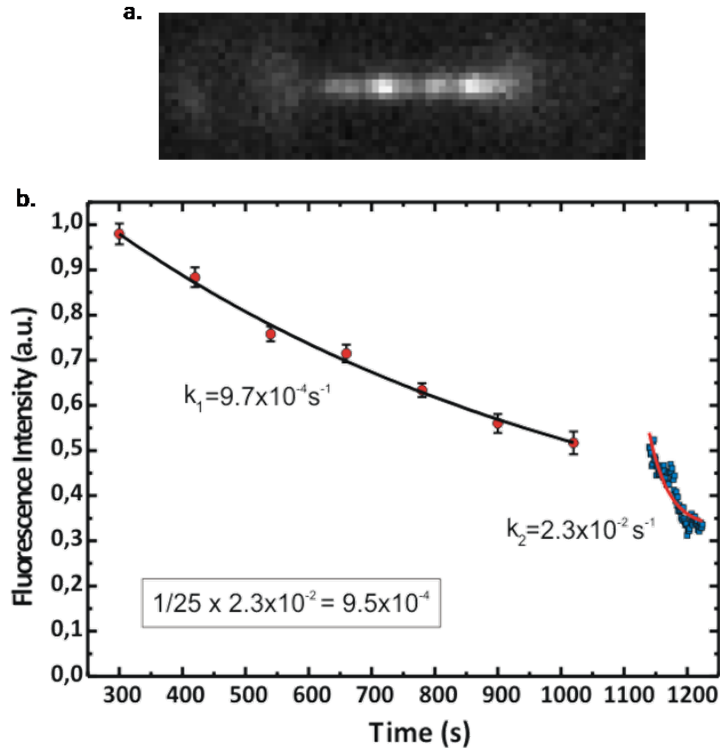


**Figure 3.1 Stability of Rad51 filament in the presence of ATP and  $\text{Ca}^{2+}$ .** a) Fluorescence image of a ssDNA molecule immediately after incubation. A ssDNA fragment was produced *in situ* by force-induced melting and incubated for 3-4 minutes in 150 nM Rad51 in the presence of ATP and  $\text{Ca}^{2+}$  (assembly buffer). After incubating, the molecule was imaged in  $\text{Ca}^{2+}$ -buffer without protein. b) Fluorescence trace of Rad51-Alexa555 bound to ssDNA. A Rad51-covered DNA molecule (shown in a) was imaged in  $\text{Ca}^{2+}$ -buffer. First strobing was applied, illuminating the molecule for 5s every 120s. Data points are average fluorescence signal  $\pm$  SD. Then, the molecule was continuously illuminated for approx. 100s. Optical density (OD) is 1.6 for both traces, corresponding to 2.5 % of total laser intensity. Fluorescence intensity is taken over full length of the DNA, is background subtracted, and normalized for number of pixels. Decay rates are obtained from single exponential fits.

## Nucleation

Filament formation is divided into three steps: nucleation, extension and disassembly and dynamics between these stages are essential for filament function. Nucleation happens when a group of proteins first attach to the DNA. The actual size of the nucleation spot has been highly debated. Previous studies have found nucleation units of 3-5 monomers on dsDNA (22) (23). These studies used Monte Carlo simulations and changes in DNA length as an indirect measure of protein binding and it is difficult to say if true recombinase binding properties were observed. Here, we directly observe binding of fluorescently labeled Rad51 proteins and we are able to localize single fluorophores with nm precision. Once the intensity of a single Rad51-Alexa555 fluorophore has been determined, we can simply 'count' the number of monomers present on a particular region of DNA. Small nucleation spots first start appearing on ssDNA after short incubations of 10-20 s with 150 nM Rad51 in assembly buffer containing 50 mM KCl. Figure 3.2.a shows a kymograph of two nucleation spots photobleaching over time. We observe between 1 and 7 nucleations on ssDNA after 30-60 s. Most prevalent were 2 nucleations ( $n=8$ ) and a maximum of 6-7 nucleations was observed only once (figure 3.2.b). Figure 3.2.c shows a stepwise bleaching trace that is characteristic for single-fluorophore bleaching. Fluorescence intensity is measured over time for a single nucleation spot (indicated with green box in figure 3.2.b). Each fluorophore persists for up to 40 s. Toward the end of the photobleaching trace, two single fluorophores bleach individually and each emits about 10,000

a.u. fluorescence. The total fluorescence signal indicates that 5-6 fluorophores have bleached in that nucleation spot. Note that the absolute fluorescence values depend on the camera settings used and on the properties of electronics in the system. We find nucleation spots with 3-7 monomers bound to the DNA after 30-60 s incubations ( $n=8$ ). The degree of labeling (DOL) of Rad51-Alexa555 is 1.3. This means that on average one out of four Rad51 molecules carries two fluorophores and that we slightly overestimate the total number of proteins. From this data we extract an average nucleation rate of  $(7 \pm 6) \times 10^{-6} \text{ s}^{-1} \text{ nt}^{-1}$  ( $n=16$ ) for Rad51 on ssDNA (histogram shown in figure 3.2.d). Similar rates have been found for Rad51 on dsDNA by other fluorescence experiments ( $4 \times 10^{-6} \text{ s}^{-1} \text{ bp}^{-1}$ ) (22). However, contrary to previous accounts, our data indicates that nucleation on dsDNA is about 5-fold slower than on ssDNA (not shown). In contrast, magnetic tweezer experiments find nucleation rates of two orders of magnitude faster on both dsDNA and ssDNA ( $4 \times 10^{-4} \text{ s}^{-1} \text{ bp}^{-1}$ ) (23).

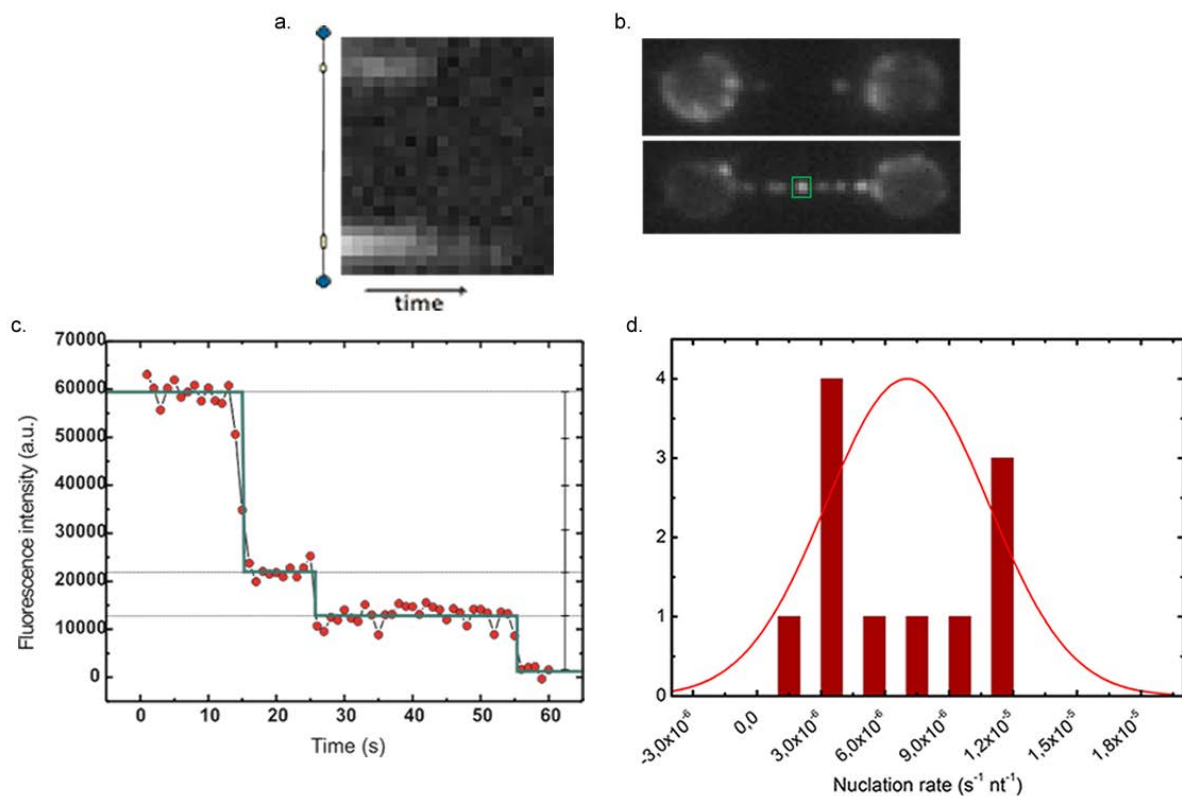


**Figure 3.2 Rad51 nucleation on ssDNA.** a) Kymograph of fluorescence intensity in time. ssDNA was created *in situ* and incubated with 150 nM Rad51 in assembly buffer. The image shows two nucleation spots photobleaching in time. b) Fluorescence images of nucleation spots on ssDNA. Small nucleation spots appear on ssDNA after 10-20 s. Top image shows 2 nucleation spots (most prevalent) and bottom image shows 6 or 7 nucleation spots (maximum). c) Photobleaching trace. Fluorescence intensity is integrated over a single nucleation spot as indicated with green box in b. Characteristic stepwise bleaching traces are observed in time. Here, 5-6 Rad51 monomers were present in a single spot. Fluorescence is background subtracted and normalized for number of pixels, OD = 0 d) Nucleation rate of Rad51 on ssDNA. ssDNA molecules were incubated for 30-60 s with 150 nM Rad51 in assembly buffer containing 50 mM KCl. Average nucleation rate is  $(7 \pm 6) \times 10^{-6} \text{ s}^{-1} \text{ nt}^{-1}$  ( $n=16$ ).

### Assembly

Once a nucleation spot has formed, free Rad51 cooperatively bind to the pre-existing filaments. In the following experiments, we studied the assembly behavior of Rad51, which includes both initial nucleation and filament growth. ssDNA molecules were incubated multiple times with Rad51 in assembly buffer and short illumination snapshots were taken after each incubation. Binding of Rad51 proteins is less cooperative than its prokaryotic homologue RecA, and Rad51 filaments form

multiple short patches on DNA. Figure 3.3.a shows fluorescence images of the filament growing in time after multiple incubations. Initially, we observe fluorescence intensity increasing in the separate nucleation spots. After longer incubations (>150s) the sizes of the patches appear to grow as well. Fluorescence traces of two different molecules are shown in figure 3.3.b. Growth rates are similar for both molecules:  $(41.8 \pm 3.4) \times 10^{-4} \text{ s}^{-1}$  and expected saturation is reached after approximately 800s. Previous experiments on dsDNA describe sigmoidal assembly behavior caused by slow nucleation (lag phase), followed by rapid extension and a final plateau phase (22). On ssDNA we observe a steady increase in fluorescence intensity followed by saturation.

### Disassembly

When Rad51 hydrolyzes ATP, it loses binding affinity for DNA and dissociates from the substrate. With our laminar flow system, we can trigger disassembly within seconds by moving the Rad51 covered DNA into  $\text{Mg}^{2+}$ /EGTA-buffer. Rad51 filaments are first formed in the presence of  $\text{Ca}^{2+}$ -ions. The chelating agent EGTA has high affinity for  $\text{Ca}^{2+}$ -ions and assists the ion-exchange inside the protein. Filament dissociation can then be followed in real time. Figure 3.4 shows photobleaching and disassembly traces at low force. First, a control experiment was done with  $\text{Ca}^{2+}$ -buffer (red dots). We have shown that the filament remains stably bound to ssDNA in the presence of  $\text{Ca}^{2+}$  for up to 900s (figure 3.1). Any fluorescence decay observed in the presence of  $\text{Ca}^{2+}$  is due to photobleaching of the Alexa555 fluorophore. In the presence of  $\text{Mg}^{2+}$ /EGTA-buffer, the fluorescence decay increases (green dots). This disassembly profile can be described with a single exponential function containing a photobleaching component and a disassembly component:

$$I = I_0 + A e^{(-x/t_1)} e^{(-x/t_2)} \quad (5)$$

and

$$k_{tot} = k_{photo} + k_{disass} \quad (6)$$

where photobleaching rate is given by  $k_{photo} = 1/t_1$  and disassembly rate is  $k_{disass} = 1/t_2$ .

The rates obtained from the traces shown are:  $k_{photo} = 3.1 \times 10^{-3} \text{ s}^{-1}$  and  $k_{tot} = 1.2 \times 10^{-2} \text{ s}^{-1}$ . According to formula (6) we find  $k_{disass} = 8.9 \times 10^{-3} \text{ s}^{-1}$ , almost three-fold faster than photobleaching under the same illumination conditions.

In addition, we probed the effects of force on disassembly. Experiments were performed at 12 pN (n=3), at 20 pN (n=3) and at 50 pN (n=2). We find that the disassembly rate decreases as force increases (figure 3.4.b). Similar results have been found on dsDNA (26). Interestingly, about one third of the molecules portray a linear disassembly profile rather than the expected exponential decay (figure 3.5.a). Linear disassembly profiles have been observed for RecA, which is known to form a continuous filament that disassembles from a single filament end (34).

### Force data

Besides directly visualizing Rad51 binding and dissociation, we are able to monitor forces induced on the ssDNA by Rad51 in real time. Figure 3.5.b shows the changes in force as the proteins assemble (left) and disassemble (right) from a ssDNA molecule. To study assembly, a ssDNA fragment was

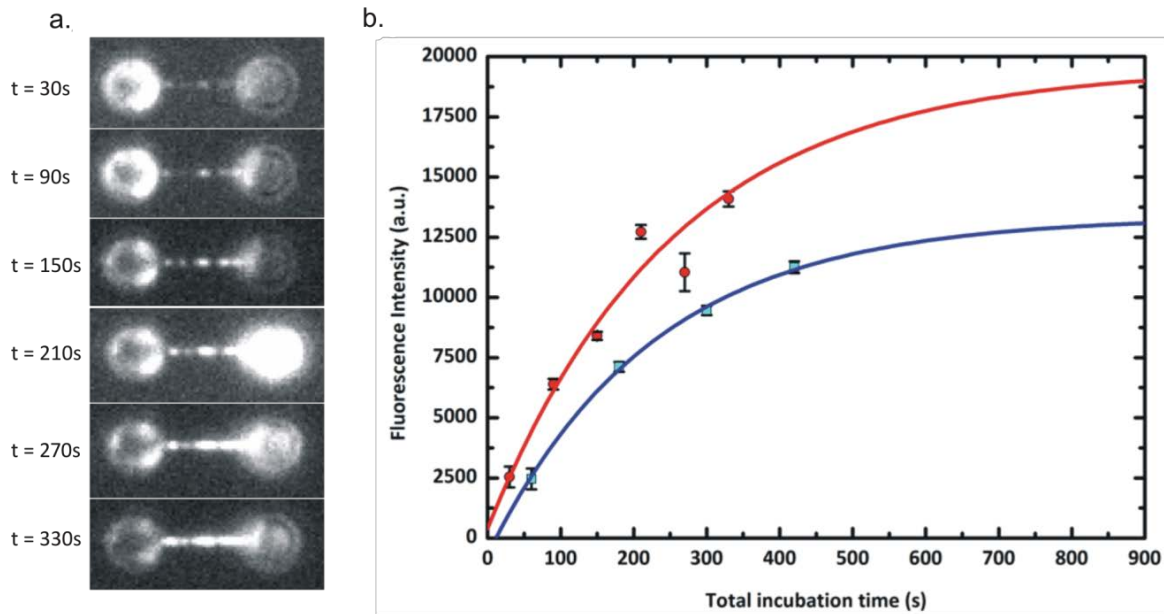


**Figure 3.3 Assembly of Rad51 filament on ssDNA. a) Fluorescence images of filament growing with time.** ssDNA was incubated multiple times with 150 nM Rad51 in assembly buffer. After each incubation, the molecule was moved into  $\text{Ca}^{2+}$ -buffer and illuminated for approximately 5s. Initially we observe fluorescence in a single nucleation spot increasing over time. The patches visually appear to grow after incubations  $t > 150\text{s}$ . **b) Fluorescence intensity trace.** Fluorescence intensity of two individual molecules increases over time after multiple incubations (molecule shown in a. is shown in red). Data points are average fluorescence signal  $\pm$  SD. Fluorescence is taken over full length of DNA, is background subtracted and normalized for number of pixels.

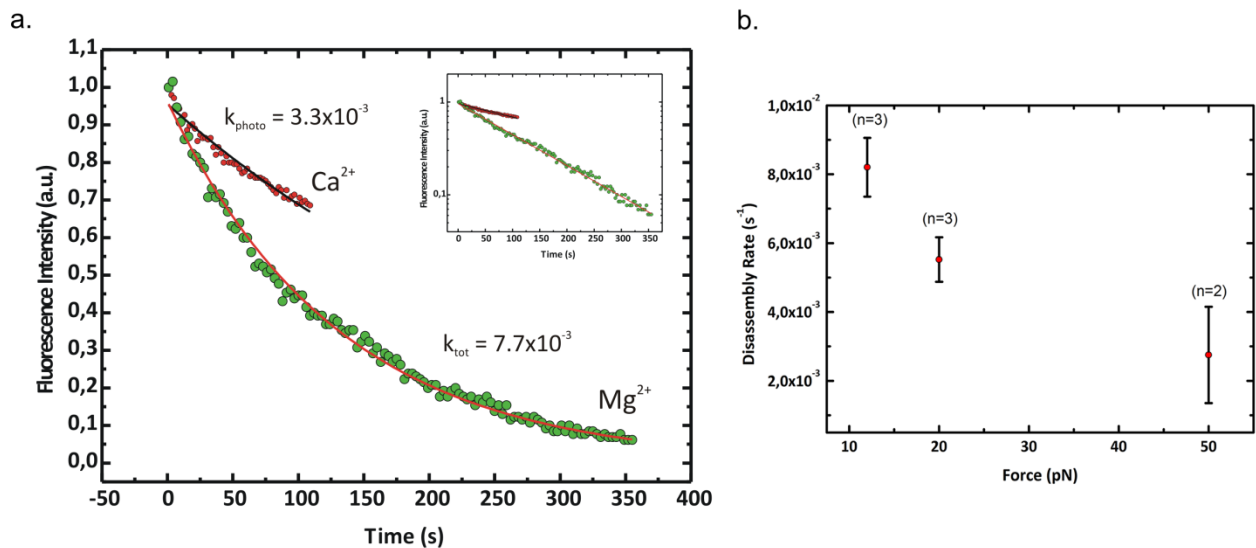


**Figure 3.4 Disassembly of Rad51 from ssDNA. a) Fluorescence intensity profile.** ssDNA was loaded with Rad51 in the presence of  $\text{Ca}^{2+}$  and then moved into  $\text{Mg}^{2+}$ /EGTA-buffer to trigger disassembly. Photobleaching trace in the presence of  $\text{Ca}^{2+}$  ( $F \sim 20$  pN) is shown in red. Disassembly trace in the presence of  $\text{Mg}^{2+}$  ( $F \sim 12$  pN) is shown in green. The same traces are shown in log scale in the upper right corner. Fluorescence is background subtracted and normalized for number of pixels and initial fluorescence intensity. OD = 1.6 **b) Disassembly rate as a function of force.** Disassembly was measured at different forces (12, 20 and 50 pN). Rates were calculated as described in the text.

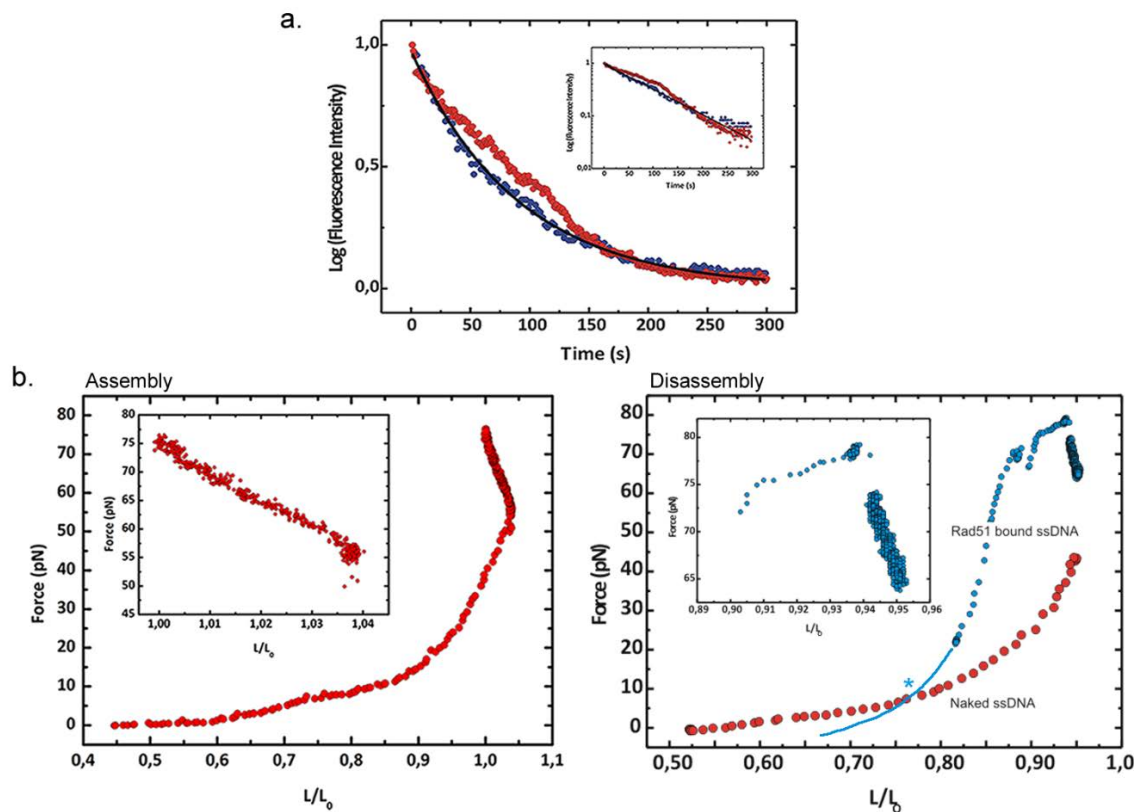


**Figure 3.5 a) Two different disassembly profiles for Rad51.** Exponential disassembly profile is observed for most molecules (shown in blue). One third of the molecules exhibit linear disassembly behavior (red trace). The traces are shown in log scale in the inset in the upper right corner. Fluorescence is background subtracted and normalized for number of pixels and initial fluorescence intensity. OD = 1.6 **b) Force-extension traces. Left: Assembly of Rad51 on ssDNA.** A ssDNA fragment caught between two optically trapped beads was incubated with Rad51 in assembly buffer at high force (55 pN). Binding of Rad51 on ssDNA is observed in real time as the DNA stiffens and shortens (inset). **Right: Disassembly of Rad51 from ssDNA.** ssDNA was incubated with Rad51 at high force (80 pN) and was then moved into  $Mg^{2+}$ / EGTA-buffer to trigger disassembly. Force-extension curves of naked ssDNA (red trace) and of Rad51-bound ssDNA (blue) are shown. As Rad51 disassembles, the DNA lengthens and its elastic stretch modulus increases (inset).

gradually pulled to 55 pN and then incubated with Rad51 in the presence of  $Ca^{2+}$ . We observe shortening of the DNA ( $\Delta L \approx 0.5 \mu m$ ) and increasing force ( $\Delta F \approx 20 pN$ ) (see inset). At 55 pN, ssDNA has a rise/bp of  $\sim 0.58$  nm. When Rad51 binds, it reconfigures the base pair distance to 150% of B-form DNA and a rise/bp of  $\sim 0.50$  nm is maintained in order to fit the DNA binding domain. Consequently we observe compression of the ssDNA. Binding is observed at extremely high forces up to 80 pN. We observe comparable behavior during Rad51 disassembly. Here, a Rad51 filament was formed on ssDNA at high force (80 pN) in the presence of ATP and  $Ca^{2+}$  and disassembly was then triggered with  $Mg^{2+}$ / EGTA (Figure 3.5.b, right panel). As the proteins detach, the force decreases and the DNA length and stretch modulus increase (blue trace, inset). The force-stretching trace will eventually cross the naked DNA trace (shown in red) when all proteins have dissociated from the substrate (crossover point is indicated with a blue star). When comparing naked DNA to Rad51-bound DNA, we observe stiffening of the DNA due to Rad51 interactions. The stretch modulus increases further as more proteins bind to the DNA and the cross-over point between the two traces moves further to the left (not shown).

## Chapter 4 Discussion

Using this novel assay, we are able to individually study the three stages of filament formation. We find that nucleation occurs with at least 3-4 Rad51 monomers, suggesting that a trimer or tetramer is the smallest nucleation binding unit. However, the values obtained in these experiments provide only a first estimate of the smallest nucleation unit. The incubation times of 30-60 s are already quite long when considering that nucleation spots first appear after only 10s at the relevant protein and salt concentrations. It is possible that some filament extension has already occurred. In addition, a degree of labeling (DOL) of 1.3 in these experiments results in a slight overestimation of the number of protein monomers bound to the DNA. Repeating the experiments with fluorescently labeled Rad51 with DOL=1 will provide more accurate values. We report an average nucleation rate of  $(7 \pm 6) \times 10^{-6} \text{ s}^{-1} \text{ nt}^{-1}$  ( $n=16$ ) for Rad51 on ssDNA. This is comparable to rates determined by fluorescence studies on double-stranded DNA (22). However contrary to previous accounts, preliminary experiments with our approach indicate that nucleation is significantly faster (~5-fold) on ssDNA than on dsDNA (data not shown). Furthermore, we observe a steady increase for assembly on ssDNA, while sigmoidal assembly traces have been described for dsDNA (22). The 5-fold difference in nucleation rates on short time-scales (<60 s) may be obscured in bulk experiments and could also explain the absence of an initial lag phase on ssDNA when compared to dsDNA. It is not yet clear from our data if the extension binding unit is monomeric or multimeric. Sufficiently short incubations and decreased protein concentration or increased salt concentration can further separate the nucleation and extension phases to clarify these issues.

In the second part of this study we show that disassembly is triggered within seconds by moving the DNA into  $\text{Mg}^{2+}$ /EGTA-buffer within our laminar flow system. Disassembly can be observed in a background-free environment in real time. We interpret the disassembly profile as a single exponent with a slow photobleaching component and a fast disassembly component. We obtain a photobleaching rate  $k_{photo} = 3.1 \times 10^{-3} \text{ s}^{-1}$  and a disassembly rate  $k_{disass} = 8.9 \times 10^{-3} \text{ s}^{-1}$  from the best traces. However, the photobleaching rate is already quite high and it is difficult to separate out the two exponential components. Using strobing (illuminating the sample in short bursts every few minutes) instead of continuous illumination can greatly improve the quality of the data in future experiments. Continuous illumination causes about 30% of the dyes to photobleach every 100s at 2.5% laser intensity (OD=1.6) and strobing decreases this by at least a factor of 10.

High tension appears to slow Rad51 disassembly from single-stranded DNA, comparable to results for disassembly from double-stranded DNA (26). On dsDNA a sigmoidal profile is observed in assembly and disassembly experiments (22) (26). On ssDNA, we do not observe an initial lag phase for both assembly and disassembly, suggesting that the binding mechanism of Rad51 to single-stranded DNA is different than on double-stranded DNA. Binding of the protein is likely influenced by the elastic properties of the DNA and further investigation is necessary to clarify these effects. Interestingly, about one third of the molecules exhibit a linear disassembly profile rather than the expected exponential behavior. Linear disassembly profiles have been observed for RecA which is known to form continuous filaments that dissociates from a single filament end. Rad51, in contrast, is known to form multiple short filaments and it is proposed that dissociation occurs from the ends of all filaments simultaneously. It is possible that a continuous filament is formed when individual short filaments come in contact with each other after long incubations. However, similar to earlier findings, Rad51 does not appear to dissociate from a single end in our experiments. During disassembly we visually observe that the filament breaks into smaller fragments that simultaneously

shrink into spots and finally disappear. The molecules that display linear behavior visually appear no different. The linear disassembly profile is observed at low and at high force and does not appear to be force-induced.

Besides fluorescence intensity, we are able to monitor forces induced by binding of Rad51 proteins in real time. ADP and slowly hydrolysable nucleotide analog ATP- $\gamma$ -S can be used to 'lock' Rad51 in its intermediate states and could provide further insights into the mechano-chemical coupling of the protein.

Reoccurring obstacles in our experimental setup are the occurrence of several noise sources that make analyzing and interpreting the data difficult. Background fluorescence does not appear to be constant inside the flow cell in the area around the DNA molecule. This effect is probably caused by proteins sticking locally to the glass cover slides. Possible solutions include blocking the flow cell surface to prevent non-specific binding of Rad51-Alexa555 or to replace flow cells more often. The DNA fragments used in these experiments are quite short and this offers some challenges as well. High fluorescence coming from the polystyrene beads produces a second source of background noise. The 'blotchy' appearance of the beads (see figure 3.3.a) suggests that a specific interaction takes place on the bead's surface. Test experiments indicate that small DNA oligos used in the biotinylation process are not properly filtered from the solution and bind to the bead's surface (data not shown). We are currently looking into improving the purification method. A crucial aspect of our analysis that is still ill-defined is the selection of a proper region of interest (ROI) along the DNA molecule. When the ROI lies too close to the bead surfaces, where the fluorophores are exposed to the high power infrared trapping laser, the overall signal is dominated by intense bleaching. Figure 4.1.a shows an example of fluorescence traces obtained from the same DNA molecule but with different ROIs. The green trace averages fluorescence over the entire length of the DNA (see inset) and yields a photobleaching rate over two-fold larger than with a region of interest far away from the beads (red trace). Another issue caused by the small size of the DNA fragments is interference between the beads when they are close together. This interference between the two beams of the dual optical trap, results in a ghost force-signal and is largest (up to 12 pN) when the distance between the beads is less than twice the bead diameter ( $\leq 2d$ ) (figure 4.2). The DNA contour length corresponds to  $\sim 1.5d$  and is within this interference region. The interference signal can be minimized by properly aligning and calibrating the system; however, these interactions must be considered when performing experiments and interpreting the data. Using a longer DNA fragment or using smaller beads may reduce these issues. Obtaining longer, nick-free DNA fragments is difficult, however, and reduces the statistical probability of obtaining a single-stranded DNA molecule.

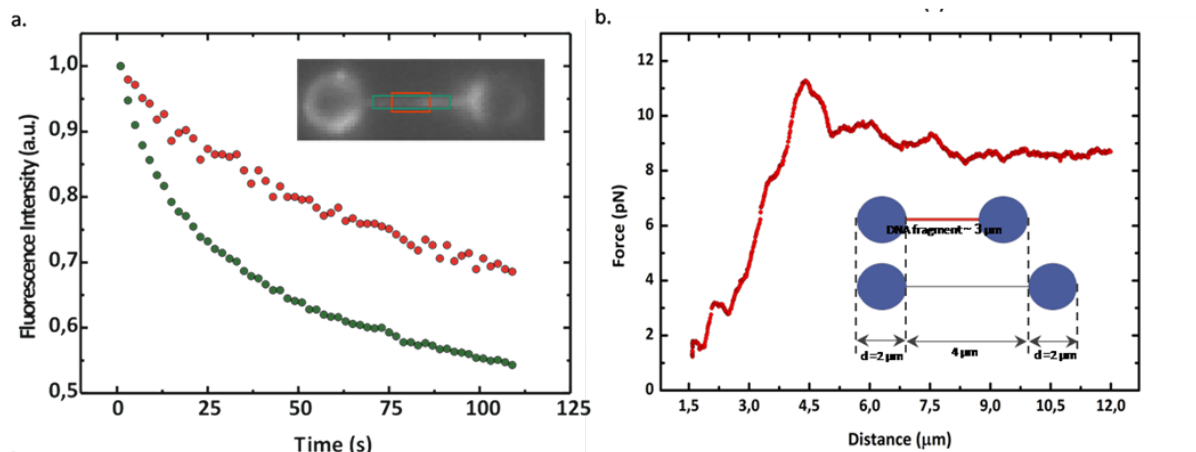


**Figure 4.1 Sources of noise. a) Selection of region of interest.** The figure shows an example of two fluorescence traces of the same molecule but with different regions of interest (ROI). The red trace is obtained for a region of interest far away from the beads (see inset top right). The green trace averages fluorescence over the entire length of the DNA. **b) Interference between beads.** Interference between the two beams of the dual optical trap is most prominent when the bead-to-bead distance is  $\leq 2d$ . The interference signal can be minimized with proper alignment and calibration of the trapping laser.

## Conclusion

Preliminary studies with this novel approach have shown that we are able to individually study the three stages of Rad51 filament formation on single-stranded DNA: nucleation, assembly and disassembly without any *a priori* assumptions. Direct observation of fluorescently labeled Rad51 proteins and high-resolution fluorescence detection provides information on protein coverage and allows direct determination of nucleation, extension and disassembly rates, as well as DNA binding unit sizes. Fluorescence data can directly be coupled to force data. Monitoring changes in force in real time allows pN detection of Rad51-induced forces and investigation of the effects of forces on filament formation. Some technical difficulties regarding background noise must still be overcome and optimization is necessary to improve the quality of the data and to obtain accurate values. Further investigation can give great insights into the mechano-chemical coupling of recombinase proteins and the exact mechanisms of strand exchange. This study probes into the mechanism of nucleoprotein filament dynamics and presents a novel approach to studying protein interactions on single-stranded DNA as a whole.

## References

---

1. *Biochemistry of homologous recombination in Escherichia coli*. **Kowalczykowski S., et.al.** 1994, Microbiological reviews, Vol. 58, pp. 401-465.
2. *Crystal structure of a Rad51 filament*. **Conway B., et.al.** 2004, Nature Struc. and Mol. Biol., Vol. 11, pp. 791-796.
3. *Immunoglobulin gene conversion: synthesizing antibody diversification and DNA repair*. **Tang E., and Martin A.** 2007, DNA repair, Vol. 6, pp. 1557-1571.
4. *Initiation of meiotic recombination by formation of DNA double-strand breaks: mechanism and regulation*. **Keeney S., and Neale M.** 2006, Biochem. Soc. Trans., Vol. 34, pp. 523-525.
5. *Mesoscale conformational changes in the DNA-repair complex Rad50/ Mre11/ Nbs1 upon binding DNA*. **Moreno-Herrero M., et.al.** 2005, Nature, Vol. 437, pp. 440-443.
6. *ATM activation by DNA double-strand breaks through the Mre11-Rad50-Nbs1 complex*. **Lee J., and Paul T.** 2005, Science, Vol. 308, pp. 551-554.
7. *gamma-H2AX and MDC1: anchoring the DNA-damage-response machinery to broken chromosomes*. **Stucki M., and Jackson S.** 2006, DNA repair, Vol. 5, pp. 534-543.
8. *DNA double-strand break repair: how to fix a broken relationship*. **Pardo B., Gomez-Gonzales B. and Aguilera A.** 2009, Cell. Mol. Life. Sci, Vol. 66, pp. 1039-1056.
9. *Mechanism of eukaryotic homologous recombination*. **San Filippo J., Sung P. and Klein H.** 2008, Annu. Rev. Biochem., Vol. 77, pp. 9.1-9.29.
10. *Mutations in yeast rad51 that partially bypass the requirement for Rad55 and Rad57 in DNA repair by increasing the stability of Rad51-DNA complexes*. **Fortin G., and Symington L.** 2002, EMBO, Vol. 21, pp. 3160-3170.
11. *Bipartite stimulatory action of the Hop2-Mnd1 complex on the Rad51 recombinase*. **Chi P., et.al.** 2007, Genes and Development, Vol. 21, pp. 1747-1757.
12. *BRCA2: a universal recombinase regulator*. **Thorslund T., and West S.** 2007, Onvogene, Vol. 26, pp. 7720-7730.
13. *Finding a match: how do homologous sequences get together for recombination?* **Barzel A., and Kupiec M.** 2008, Nature reviews Genetics, Vol. 9, pp. 27-37.
14. *Improving the chances of finding the right partner*. **Moore G., and Shaw P.** 2009, Curr. Opin. in Gen. and Develop., Vol. 19, pp. 99-104.
15. *Rapid exchange of A:T base pairs is essential for recognition of DNA homology by human Rad51 recombination protein*. **Gupta R., et.al.** 1999, Molecular Cell, Vol. 4, pp. 705-714.
16. *Rad52 promotes second-end DNA capture in double-stranded break repair to form complement-stabilized joint molecules*. **Nimonkar A., Sica A., and Kowalczykowski S.** 2009, PNAS, Vol. 106, pp. 3077-3082.
17. *The bacterial RecA protein as a motor protein*. **Cox M.** 2003, Annu. Rev. Microbiol., Vol. 57, pp. 551-577.

18. *Inter-subunit interactions that coordinate Rad51's activities.* **Grigorescu A., et.al.** 2009, Nucl. Acids Res., Vol. 37, pp. 557-567.
19. *Structural analysis of the human Rad51 protein-DNA complex filament by tryptophan fluorescence scanning analysis: Transmission of allosteric effects between ATP binding and DNA binding.* **Renodon-Corniere A., et.al.** 2008, JMB, Vol. 383, pp. 575-587.
20. *Direct observation of individual RecA filaments assembling on single DNA molecules.* **Galletto R., Amitani I., Baskin R. and Kowalczykowski S.** 2006, Nature, Vol. 443, pp. 875-878.
21. *Fluorescent human Rad51 reveals multiple nucleation sites and filament segments tightly associated along a single DNA molecule.* **Modesti M., et.al.** 2007, Cell Structure, Vol. 15, pp. 599-609.
22. *Direct imaging of human Rad51 nucleoprotein dynamics on individual DNA molecules.* **Hilario J., Amitani I., Baskin R. and Kowalczykowski S.** 2009, PNAS, Vol. 106, pp. 361-368.
23. *Real-time assembly and disassembly of human Rad51 filaments on individual DNA molecules.* **Heijden van der T., et.al.** 2007, NAR, Vol. 35, pp. 5646-5657.
24. *Real-time observation of RecA filament dynamics with single monomer resolution.* **Joo C., et.al.** 2006, Cell, Vol. 126, pp. 515-527.
25. *Domain structure and dynamics in the helical filament formed by RecA and Rad51 on DNA.* **Yu X., et.al.** 2001, PNAS, Vol. 98, pp. 8419-8424.
26. *Counting Rad51 proteins disassembling from nucleoprotein filaments under tension.* **Mameren van J., et.al.** 2008, Nature, pp. 1-4.
27. *Motoring along with the bacterial RecA protein.* **M. Cox.** 2007, Nature reviews Moll. Cell Biol., Vol. 8, pp. 127-138.
28. *Unraveling the structure of DNA during overstretching by using multicolor, single-molecule fluorescence imaging.* **van Mameren J., et.al.** 2009, PNAS, Vol. 106, pp. 18231-18236.
29. *Salt dependence of the elasticity and overstretching transition of single DNA molecule.* **Wenner J., et.al.** 2002, Biophys. J., Vol. 82, pp. 3160-3169.
30. *Polymerization and mechanical properties of single RecA-DNA filaments.* **Hegner M., Smith S., and Bustamante C.** 1999, Proc. Natl. Acid. Sci. USA, Vol. 96, pp. 10109-10114.
31. *Optical trapping.* **Neuman K., and Block S.** 2004, Rev. Sci. Instrum., Vol. 75, pp. 2787-2809.
32. **Williams M.** Optical tweezers: Measuring piconewton forces. *Biophysics Textbook Online.* s.l. : Biophysical society, 2002.
33. *Power spectrum analysis for optical tweezers. II: Laser wavelength dependence of parasitic filtering, and how to achieve high band-width.* **Berg-Sorensen K., Peterman E., Weber T., Schmidt C., and Flyvbjerg H.** 2006, Rev. of Scient. Instrum., Vol. 77, p. 063106.
34. *Dynamics of RecA filaments on single-stranded DNA.* **Loenhout M., et.al.** s.l. : NAR, 2009, pp. 1-11.

## Appendix

---

### DNA construct and protein preparation

*E. coli* novablue competent cells were transformed with pKYB1 expression vector and grown in LB + 50 µg/ ml kanamycin. The plasmid was purified with HiSpeed midi plasmid purification kit. EcoRI restriction enzyme was added to specifically cut open the plasmids and the fragments were labeled on the 3'-end with biotin-14-dATP in the presence of Klenow exo-polymerase. Samples were incubated for 1-2 h at 37°C and purified with Microcon YM-50 columns. Subsequently, samples were incubated for 60-75' at 37°C with KpnI fastdigest to remove the 3'-end of the second biotinylated strand. A second purification step with YM-50 columns was performed to remove the small biotinylated oligos. Specially designed KpnI primers containing 25 nt overhang were added at 60x excess. T4 ligase ligates primers to 5'-end of the biotinylated strand and samples were incubated for 2h at RT. Prior to addition of T4 ligase, samples were incubated for 3' at 55°C to prevent aggregation. Finally, samples were purified, diluted in TNT buffer and stored at -20°C. (See also figure 2.3)

Human Rad51-Alexa555 was provided by Mauro Modesti and was purified and labeled as described elsewhere (21). Degree of labeling (DOL) is 1.3. Aliquots were stored at -80°C and were flash-frozen with liquid nitrogen after use. All experiments used protein concentration of 100-150 nM unless stated otherwise.

### Buffers

20 mM tris-HCl (pH7.5) + 50 mM KCl + 1 mM DTT buffer was used in all experiments. DTT (reducing agent) was stored at -20°C and was added fresh to each sample.

Assembly buffer: buffer + 0.5 mM ATP + 1 mM CaCl<sub>2</sub>

Imaging buffer: buffer + 1 mM CaCl<sub>2</sub>

Disassembly buffer: buffer + 10 mM MgCl<sub>2</sub> + 10 mM EGTA (chelating agent)

100-150 nM Rad51-Alexa555 was added to assembly buffer and mixed by resuspending right before measurements. Imaging buffer was used in all nucleation and assembly experiments. Disassembly buffer was used in all disassembly experiments.

### Experimental procedure

The optical trapping/ fluorescence microscopy setup was calibrated with power spectrum analysis prior to measuring. Sample syringes and flow cell chambers were extensively flushed with water before and after each experiment. Each sample was assigned a sample syringe as follows: Ch 1: bead solution, Ch 2: DNA solution, Ch 3: Imaging or Disassembly buffer, Ch 4: protein solution (figure 2.2). Channel designations were maintained to prevent contamination and protein aggregation. Samples were deoxygenated and infused with nitrogen prior to experiments to prolong fluorophore and DNA lifetime.

A biotinylated dsDNA fragment was caught between two streptavidin-covered beads. The distance between the beads was increased by moving one of the traps and force was increased beyond the overstretching plateau to produce single-stranded DNA. Beads with diameter of 2 µm were used in all experiments. The ssDNA molecule was moved into the protein channel and incubated with Rad51. After incubation, the DNA fragment was moved into buffer channel and illuminated with 532 nm fluorescence excitation laser. Camera readout was triggered externally to reduce photobleaching.